Biosensors and Bioelectronics 298 (2026) 118382

Contents lists available at ScienceDirect

Biosensors and Bioelectronics

journal homepage: www.elsevier.com/locate/bios

Engineered bacterial S-layer enhanced high electron mobility transistor sensors for ultrasensitive detection of tumor antigen

Jingya Tang [a,g,1], Chenyang Yang [a,g,1], Jianwen Sun [c], Zhe Li [d], Yue Men [a,f], Zewen Liu [c], Guoqi Zhang [e], Xian-En Zhang [b,a,*], Dian-Bing Wang [a,**]

[a] State Key Laboratory of Biomacromolecules, Institute of Biophysics, Chinese Academy of Sciences, Beijing, 100101, China
[b] Faculty of Synthetic Biology, Shenzhen University of Advanced Technology, Shenzhen, 518055, China
[c] School of Integrated Circuits, Tsinghua University, Beijing, 100084, China
[d] Precision Scientific (Beijing) Co. Ltd., Beijing, 100085, China
[e] Department of Microelectronics, Delft University of Technology, 2628 CD, Delft, the Netherlands
[f] School of Life Sciences, Fujian Agriculture and Forestry University, Fuzhou, 350002, China
[g] University of Chinese Academy of Science, Beijing, 100049, China

ARTICLE INFO

Keywords:
S-layer
HEMT
Tumor antigen
Ultrasensitive detection

ABSTRACT

Ultrasensitive and specific detection of low-abundance tumor biomarkers remains a major challenge for early and minimally invasive cancer diagnosis. Here, we present a high-performance biosensing platform that integrates a genetically engineered bacterial S-layer with an AlGaN/GaN high-electron-mobility transistor (HEMT) sensor for label-free detection of tumor antigens. As a proof-of-concept, the ovarian cancer antigen human epididymis protein 4 (HE4) was selected. Specifically, the S-layer protein rSbpA was fused with HE4-specific nanobody 1G8 to construct a bifunctional membrane capable of self-assembling into an ordered bio-recognition layer on the sensor surface. Compared to conventional chemical crosslinking, S-layer-driven assembly increased antibody loading by 50 % and minimized nonspecific adsorption in plasma environments. The resulting HEMT sensor detected HE4 across a dynamic linear range (10^{-21} to 10^{-14} M), identifying patients with ovarian cancer with 100 % diagnostic accuracy (AUC = 1.0). This study establishes a versatile and modular biosensing strategy for ultra-low-abundance biomarker detection with broad potential applications in the precision diagnostics of cancer and other diseases.

1. Introduction

Tumor antigens are molecules that are either produced by tumors or generated in response to tumor development (Zhou et al., 2024). These antigens play critical roles in tumorigenesis, including the regulation of cell proliferation, evasion of apoptosis, immune escape, and metastasis (J. et al., 2008). Advances in tumor immunology have led to the identification of numerous tumor antigens as potential diagnostic markers. Accordingly, the detection of circulating biomarkers in the bloodstream has emerged as a valuable strategy for early and minimally invasive cancer diagnosis, which requires highly sensitive detection methods. Conventional detection techniques such as enzyme-linked immunosorbent assays (Liu et al., 2021) (ELISA) and chemiluminescence immunoassays (Zhang et al., 2016) (CLIA) have been widely used in clinical diagnostics. However, their limited sensitivity often restricts their application in early-stage disease detection, in which target biomarkers are present at ultralow concentrations (below pM)(Wu et al., 2019).

Field-effect transistor (FET) biosensors, which are three-terminal devices that operate by modulating channel conductivity through an electric field, offer promising alternatives (Kaisti, 2017). When target biomolecules bind to the recognition elements immobilized on the FET gate surface, the resulting change in local charge distribution gates the channel, converting the biomolecular interactions into measurable electrical signals. High electron mobility transistors (HEMT) are a prominent class of FET sensors, the AlGaN/GaN heterostructure consist

* Corresponding author. Faculty of Synthetic Biology, Shenzhen University of Advanced Technology, Shenzhen, 518055, China.
** Corresponding author.
E-mail addresses: zhangxe@ibp.ac.cn (X.-E. Zhang), wangdb@moon.ibp.ac.cn (D.-B. Wang).
[1] These authors contributed equally.

https://doi.org/10.1016/j.bios.2026.118382
Received 16 September 2025; Received in revised form 5 January 2026; Accepted 7 January 2026
Available online 8 January 2026

of high density and mobility of the two-dimensional electron gas (2DEG) at the interface, which exhibits superior sensing characteristics and is therefore utilized in high-sensitivity biosensing (Hemaja et al., 2022).

FET biosensors have gained significant attention owing to their high sensitivity in detecting viruses (Seo et al., 2020; Yang et al., 2024), antigens (Wu et al., 2020) antibodies (Kang et al., 2021), and nucleic acids (Zhang et al., 2024; Hwang et al., 2020) Because biorecognition elements mediate the binding between target biomolecules and the sensing interface, homogeneous and high-density immobilization is essential for achieving high-performance sensing. Therefore, the rational and precise design of bio-recognition elements in an arrangement has become an effective approach for developing highly sensitive and specific FET biosensors (Zhang et al., 2023). For example, Yang et al. developed an N-terminal functionalization strategy to address the challenges posed by random orientations in C-terminal modifications, enabling a more uniform arrangement of recognition elements and achieving a linear detection range spanning five orders of magnitude (10^{-16} to 10^{-12} g/mL) (Yang et al., 2022). In another study, sensing surfaces were functionalized using chemically self-assembled monolayers (SAMs) and biologically oriented protein adapters, allowing for controlled molecular configurations and orientations (Guo et al., 2023). Despite these advances, several significant challenges remain. Many functionalization strategies rely on chemical reactions that may compromise the biological activities of the recognition elements. Furthermore, FET biosensors, typically HEMT biosensors, exhibit a relatively narrow linear dynamic range (Sarangadharan et al., 2018; Woo et al., 2020), which limits their quantitative accuracy across broad analyte concentrations. Addressing these limitations is crucial for advancing FET biosensing platforms.

The S-layer, a two-dimensional protein lattice found in bacteria and archaea, has emerged as a powerful platform for biosensing applications (Schuster, 2018). S-layer proteins possess highly ordered crystalline symmetry (Grill, 2025; Pallares, 2022), defined pore size (Lavinia, 2024; Moll, 2002), and intrinsic capacity for forming oriented and anti-fouling monolayers on diverse substrates (Sleytr et al., 2007), which collectively make them an exceptional biological scaffold for surface functionalization and sensing. An S-layer-based approach was employed to construct biomimetic systems with uniform nanostructures and precisely controlled arrangements of functional domains (Qing et al., 2023). In our previous work, we utilized the S-layer from *Bacillus anthracis* as a nanocarrier for enzyme loading and constructed functional nanoarrays for the serological diagnosis of anthrax (Wang et al., 2015). Further, by combining a genetically encoded SpyTag/SpyCatcher system with a redesigned S-layer, we developed a high-quality gold-based biosensing interface that can serve as a versatile platform for protein immobilization (Tang et al., 2022). This work illustrates the suitability of S-layer architectures for creating well-defined sensing interfaces, building on these findings, we further exploit the intrinsic self-assembly properties of S-layer proteins to construct an ordered interface on a more sensitive biosensor platform.

In this study, we present a label-free and ultrasensitive strategy for detecting tumor antigens by integrating an artificial bacterial S-layer with an HEMT sensor. Specifically, a truncated S-layer protein was fused to a nanobody to target a tumor-specific antigen. The recombinant protein was engineered to self-assemble on HEMT sensor surfaces, maximizing the nanobody packing density within the confined sensing areas. Using this approach, we achieved highly sensitive and specific detection of the ovarian cancer biomarker human epididymis protein 4 (HE4) across a concentration range of 10^{-21} M to 10^{-14} M. Clinical validation using plasma samples from patients with ovarian cancer and healthy individuals confirmed the sensor's excellent diagnostic accuracy and strong potential for clinical application. In addition to HE4 detection, this S-layer-based HEMT strategy offers a robust and versatile platform for developing novel biosensors that target a wide array of disease biomarkers, thereby advancing the field of precision diagnostics.

2. Materials and methods

2.1. Plasmid, strains, and reagents

Plasmid pET28a was used for gene insertion and expression. Recombinant plasmids were amplified in *Escherichia coli* DH5α, and recombinant proteins were expressed in *E. coli* Rosetta (DE3). S-layer protein from *Lysinibacillus sphaericus* CCM2177 was selected,the plasmid pET28a-rSbpA was constructed in our lab (Tang et al., 2022). The pEASY®-Basic Seamless Cloning and Assembly Kit (CU201) used for gene cloning was purchased from TransGen (China). The recombinant human HE4 (12609-H08H) was purchased from SinoBiological Co. All other reagents were of analytical grade. All aqueous solutions were prepared using deionized water.

2.2. Protein expression and purification

Full-length 1G8 genes (372 bp) were commercially synthesized and inserted into pET28a-rSbpA to construct the plasmid pET28a-rSbpA-1G8. The amino acid sequence (GSGSGSGSGSGS) was introduced as a linker connecting the S-layer protein and the HE4 nanobody 1G8.The expression and purification of rSbpA-1G8 was performed as described in the previous study (Tang et al., 2022).

2.3. Characterization of self-assembled recombinant SbpA-1G8 protein

Transmission electron microscopy (TEM) was employed to evaluate the self-assembly properties of recombinant rSbpA-1G8 in solution. Purified rSbpA-1G8 (1 mg/mL) was dialyzed against deionized water containing 10 mM $CaCl_2$ for 24 h at 20 °C. Self-assembled products (5–10 μL) were deposited onto discharged TEM grids and imaged using an FEI Tecnai20 microscope operated at 200 kV.

For AFM analysis, dialyzed proteins were drop onto a clean gold substrate for self-assembly and imaged under liquid conditions.

The self-assembled recombinant S-layer proteins on gold electrodes were characterized by X-ray photoelectron spectroscopy (XPS) to analyze the elemental composition (C and N). The electrochemical performance was assessed by cyclic voltammetry and electrical impedance spectroscopy using an electrochemical workstation. A gold electrode served as the working electrode, with an Ag/AgCl (saturated KCl) reference electrode and a platinum counter electrode. The supporting electrolyte consisted of 10 mM $K_3[Fe(CN)_6]$ solution in 0.1 M KCl.

2.4. Fabrication of AlGaN/GaN HEMT device

The AlGaN/GaN HEMT device was fabricated following a previously reported method (Yang et al., 2024). Device fabrication starts with mesa etching to define the active region, followed by deposition of Ti/Al/-Ti/Au (20/110/40/50 nm) ohmic contacts via evaporation and rapid thermal annealing at 870 °C for 45 s under nitrogen. A 200 nm SiO_2 layer is then deposited by plasma-enhanced chemical vapor deposition (PECVD) for interlayer isolation, and Ti/Au/Ti (10/300/10 nm) is deposited as source–drain interconnects. Subsequently, 100/200 nm SiO_2/Si_3N_4 passivation layers are deposited by PECVD. Contact pads and gate windows are opened by inductively coupled plasma etching and buffered oxide etchant treatment. Finally, a Ti/Au (2/10 nm) layer is patterned in a 600 μm × 600 μm gate region as the sensing area, and a 6 μm-thick benzocyclobutene layer is patterned as an insulating layer. An AlN interlayer (1 nm) is inserted between GaN and AlGaN to reduce dislocation density and enhance electron mobility. In this architecture, the GaN cap layer functions as the dielectric layer, while the Au layer serves as the biofunctionalization interface.

2.5. SPR measurement

Surface plasmon resonance (SPR) measurements were performed

using a BIAcore 3000 instrument. Bare gold chips were used for protein immobilization.

For S-layer self-assembly, the purified rSbpA-1G8 in 50 mM Tris-HCl (pH 9.0), 150 mM NaCl, and 10 mM $CaCl_2$ was injected onto the gold chip at a flow rate of 10 μL/min to facilitate self-assembly. For chemical crosslinking, gold chip was modified with 50 mM 11-Mercaptoundecanoic (11-MUA) overnight, followed by surface activation using N-(3-(dimethylamino)propyl)-N′-ethyl-carbodiimide hydrochloride (EDC) and N-hydroxysuccinimide (NHS). The rSbpA-1G8 was then immobilized for 30 min, and remained sites were blocked with ethanolamine. Phosphate-buffered saline with 0.05 % Tween-20 (PBST) was used for baseline establishment and washing.

Protein immobilization was quantified by recording changes in response units (RU), defined as the difference before and after immobilization.

2.6. Functionalization of HEMT sensing surface by engineered S-layer

The fabricated HEMT devices were exposed to UV radiation for 15 min, then cleaned with piranha solution (H_2O_2:H_2SO4 = 3:7) for 1 min. Subsequently, the sensors were thoroughly rinsed with deionized water and dried under nitrogen gas. The concentration of the purified recombinant S-layer protein was adjusted to 1 mg/mL in 50 mM Tris-HCl (pH 9.0), 150 mM NaCl, and 10 mM $CaCl_2$. The S-layer protein solution was then dropped onto the sensor surface and allowed to self-assemble overnight at 4 °C.

The chemical crosslinking of rSbpA-1G8 on the HEMT sensors followed a procedure similar to that used for the SPR measurements. A solution of 11-MUA was used to introduce the carboxylic acid groups, then activated using the mixture of EDC and NHS for 1 h at room temperature. After thoroughly rinsing with ethanol and deionized water to remove excess reagents, the HEMT device was incubated with rSbpA-1G8 (1 mg/mL) for 3 h. Subsequently, nonspecific binding sites were blocked using 1 mg/mL BSA for 1 h.

2.7. Electrical characterization of AlGaN/GaN HEMT device

Electrical characterization of the HETM device was performed using a Keithley sourcemeter (2614 B), which supplied the drain and gate voltages. An Ag/AgCl electrode was used to provide the liquid gate voltage through the solution.

In the transfer characteristic curves measurement, Gate–Source Voltage (V_{GS})was set to range from −2 V to 1 V, while Drain–Source Voltage (V_{DS})was maintained at 0.5 V. For output characteristics measurements, V_{DS} was set to range from −1 V to 1 V, and V_{GS} was varied from −2 V to 2 V. Data recording was performed only after signal stabilization before each test. All measurements were performed in ddH_2O.

2.8. HE4 protein and clinical sample test

Clinical plasma samples from patients with ovarian cancer and healthy individuals were obtained by centrifuging whole blood at 3000×*g* for 30 min. 10 μL of 10-fold diluted plasma was incubated with the sensor chips for 15 min.

HE4 protein solutions were serially diluted and incubated with the sensor chips for 15 min. After incubation, all samples were rinsed to remove unbound proteins, and transfer curve measurements were performed in ddH_2O. Transfer characteristic curves were recorded to calculate the potential shifts.

For non-specific binding signal assessment, BSA or plasma at different concentrations, HER2, CD106, and CD80 (each at 10 ng/mL), human serum albumin (HSA, 60 mg/mL) and human immunoglobulin G (IgG, 20 mg/mL) was incubated with the HEMT sensor for 15 min, followed by removal and subsequent transfer curve measurement. The matrix effect was assessed by the artificial plasma at different dilution.

3. Results and discussion

3.1. Design and fabrication of bacterial S-layer-based HEMT sensors

As illustrated in Fig. 1a, the S-layer protein rSbpA from *Lysinibacillus sphaericus* CCM2177 was selected, the HE4-specific nanobody 1G8 (Yu et al., 2022) (124 amino acids) is genetically fused to the S-layer protein via a flexible linker. The self-assembly properties of rSbpA facilitated the formation of a two-dimensional antibody nanostructure within the sensing area (Fig. 1b). This approach offers two key advantages: (i) the uniform immobilization of nanobodies forms controlled biorecognition elements on the sensor surface and (ii) the self-assembled rSbpA-1G8 significantly increases the nanobody density per unit area, enhancing the target capture efficiency. Furthermore, the formation of a dense protein membrane effectively suppresses non-specific binding, thereby improving the overall sensitivity and specificity of the HEMT sensor.

As illustrated in Fig. 1c, the AlGaN/GaN HEMT sensor chip comprises the source, drain electrodes, and sensing area. The patterned AlGaN/GaN channel is positioned between the source and drain electrodes, and the insulating layer on the left side provides electrode encapsulation. Gold (Au) is coated on the sensing area because of its excellent biocompatibility and suitability for biomolecular modification.

The presence of a specific tumor antigen triggers an antigen-antibody interaction upon the antigen binding to the immobilized nanobody on the sensor surface, the local charge distribution near the transistor channel changed consequently. In parallel, counter ions in the electrical double layer redistribute to screen for new charges, further affecting the gate potential sensed by the HEMT device. These effects cause a shift in the gate voltage (Vg). This regulates the channel current (I_{DS}), as expressed in Eq. (1):

$$I_{DS} = C_{OX}\mu\frac{W}{L}\left[\left(V_g - V_{TH}\right)V_{DS} - \frac{1}{2}V_{DS}^2\right] \quad (1)$$

where μ refers to the HEMT carrier mobility, W and L represent the gate width and length, respectively, *Cox* is the gate-to-channel capacitance, V_{TH} is the threshold voltage, and V_{DS} is the drain-source voltage. By monitoring the changes in $V_{g,}$ the presence and concentration of HE4 can be quantitatively assessed.

A critical factor in FET-based biosensing is the Debye length (λ_D), which defines the effective range over electrical charges in a solution can influence the electric field at the gate surface (Vacic et al., 2011). The Debye length is inversely related to the ionic strength of the electrolyte solution and is expressed as follows:

$$\lambda_D = \frac{1}{\sqrt{4\pi l_B \sum_i \rho_i z_i^2}} \quad (2)$$

where l_B is the Bjerrum length (0.7 nm), and ρ_i and z_i are the density and valence of the *i*-th ionic species, respectively. Under physiological ionic conditions (e.g., 1 × PBS), λ_D is about 0.7 nm (Chu et al., 2017), rendering the analyst undetectable beyond this screening distance. To address this limitation, we conducted measurements in deionized water and employed compact nanobodies (2–4 nm (Karami et al., 2020) in size) as binding elements. This strategy minimizes the impact of the Debye length on detection sensitivity and retains the target charges within the sensing zone. We reasoned that integrating nanobodies into the S-layer scaffold would be more efficient than incorporating full-length antibodies (~10 nm (Reth, 2013)), because previous studies coupling large-sized components (including GPCRs, IgG-Fc domains, and Protein A) to S-layer proteins achieved only nanomolar sensitivities using FET-based sensors (Qing et al., 2023). In addition, nanobodies exhibit exceptional conformational stability (Chen et al., 2021) and retain their binding function after thermal stress (Kakasi et al., 2023), making them well suited for robust diagnostic applications.

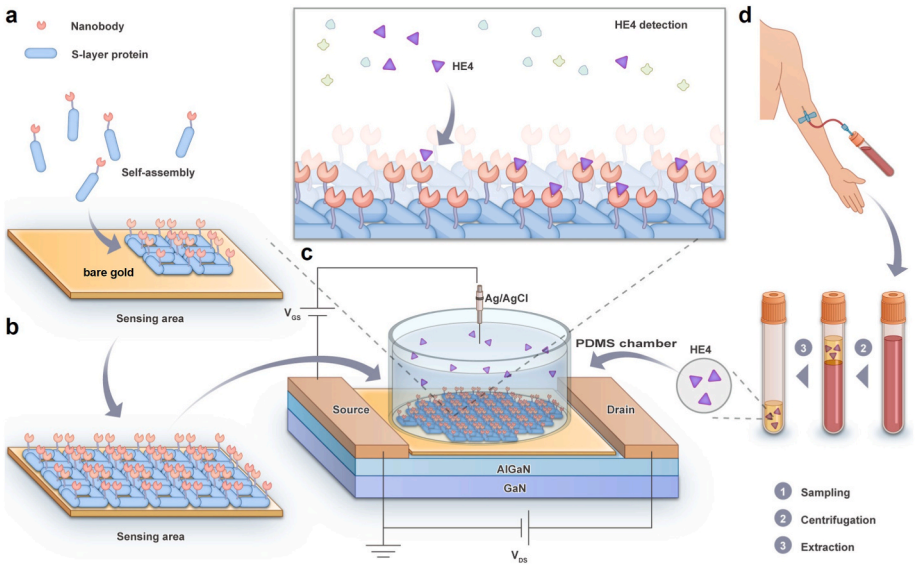

Fig. 1. Layout of ultra-sensitive detection system integrated by redesigned S-layer protein and HEMT sensor. (a) Schematic of the recombinant S-layer protein fused by rSbpA and nanobody 1G8. (b) The self-assembly of rSbpA-1G8 on the HEMT sensor surface. (c) Illustration of the detection of HE4 on S-layer based HEMT sensor. (d) The extraction of plasma from patients with ovarian cancer.

3.2. Engineering and characterization of bacterial S-layer on gold electrodes

For the engineering of bacterial S-layer, the recombinant S-layer protein rSbpA-1G8 was successfully expressed in *E. coli*. The purified protein had an approximate molecular weight of 124 kDa, as confirmed by Fig. S1. To investigate the self-assembly properties of rSbpA-1G8 in solution, transmission electron microscopy (TEM) was employed. As shown in Fig. 2a, rSbpA-1G8 formed a monolayer membrane after self-assembly. These results demonstrated the self-assembly capability of the recombinant S-layer protein and confirmed the successful formation of nanobody-based nanomembranes. The self-assembled rSbpA-1G8 layer serves as a biomolecular immobilization scaffold, enabling uniform and oriented nanobody immobilization. Upon specific antigen–nanobody binding, changes in the interfacial charge distribution are subsequently converted into electrical signals by the sensor.

In our previous study, we confirmed that a recombinant S-layer protein effectively functionalized a gold-based sensor surface through self-assembly (Tang et al., 2022). Here, the concentration of purified rSbpA-1G8 was adjusted to 1 mg/mL in the assembly buffer, followed by self-assembly on cleaned gold electrodes. To further evaluate the functionalization of rSbpA-1G8 on the gold electrodes, X-ray photoelectron spectroscopy (XPS) was performed. As shown in Fig. 2b, the XPS spectrum revealed a significant enhancement in the C 1s signal intensity after

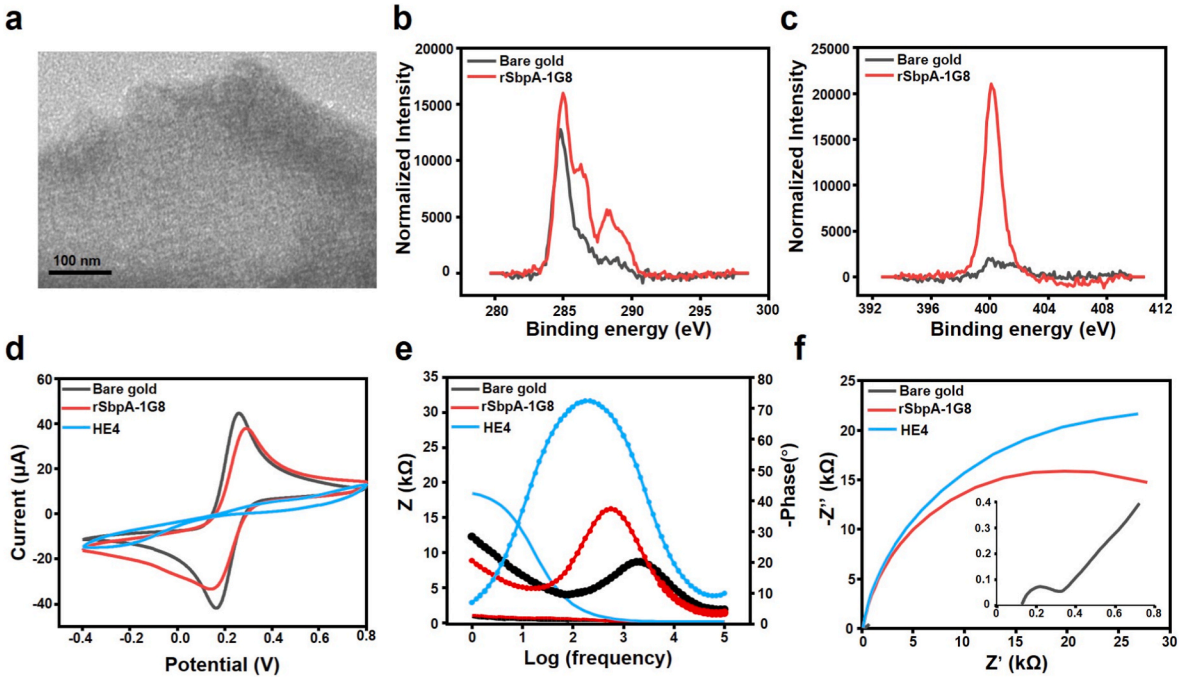

Fig. 2. Characterization of the self-assembled rSbpA-1G8 in solution and on gold electrode. (a) TEM image of the self-assembly products of rSbpA-1G8 in solution. (b) High-resolution XPS spectra for C 1s, and N 1s (c) of the gold electrode and rSbpA-1G8 modified electrode. CV curves(d), Nyquist plots (e), and Bode plots (f) for the pristine Au electrode and modified electrodes.

the assembly of the recombinant S-layer protein. The dominant peak near 285 eV corresponds to C-C/C-H bonds arising from aliphatic chains or hydrophobic moieties in the protein. A weak peak in the 288–290 eV range suggests the presence of C-O or C=O bonds, further supporting the successful immobilization of the engineered S-layer on the gold electrode. Additionally, the appearance of the N 1s peak further confirmed the presence of a protein layer (Fig. 2c). Cyclic voltammetry (CV) and electrochemical impedance spectroscopy (EIS) were used to evaluate the electrical properties of the gold electrodes. The bare gold electrode presented well-defined reversible redox peaks, with a reduction peak current of 41.7 μA, an oxidation peak current of 44.6 μA, and a peak-potential separation of 100 mV. Upon self-assembly of rSbpA-1G8 on the electrode surface, the peak current decreased, and the peak-to-peak separation widened, indicating reduced ion permeability due to the protein layer. Moreover, after the binding of HE4 to nanobody 1G8, the penetration of the redox probe during the scanning time was further hindered, resulting in a near-complete suppression of the current (Fig. 2d and e). Consistently, Fig. 2f shows a significant increase in the semicircle diameter in the high-frequency region after the self-assembly of rSbpA-1G8 on the gold electrode, reflecting increased electron transfer resistance.

Collectively, these results confirmed the successful immobilization of SbpA-1G8 on the gold electrode via self-assembly and demonstrated that the nanobody on the electrode retained its binding activity toward the tumor antigen HE4.

3.3. Electrical performance of HEMT sensor

The fabricated HEMT sensor is shown in Fig. S2, the sensing area of the HEMT biosensor is 600 × 600 μm^2. We first evaluated the electrical performance of the HEMT sensor before biofunctionalization. Transfer characteristic curves were measured in solutions with different ionic strengths. As shown in Fig. 3a, the transfer characteristic curves exhibit a rightward shift with increasing ionic concentration. Notably, a potential shift of 136 mV was observed in the 10 mM PBS solution compared to that in H_2O (Fig. 3b). A similar consecutive rightward shift in the transfer characteristic curves was observed when testing solutions with different pH values (Fig. 3c). Furthermore, the output characteristic curves were measured under varying V_{DS}, demonstrating that I_{DS} changes with different V_{DS}. Both the initial measurement (Fig. 3d) and the 100th operational cycle (Fig. 3e) showed consistent behavior. It can also be observed from Fig. 3f that the HEMT sensor exhibits a negligible potential shift over 100 continuous transfer measurement cycles. From the transfer characteristics, the key device parameters were extracted to assess the electronic quality of the fabricated AlGaN/GaN HEMT sensor. The transconductance (g_m) was determined to be approximately 0.24 ms (Fig. S3), and the electron mobility of the two-dimensional electron gas (2DEG) at 25 °C were calculated to be 1500 $cm^2\ V^{-1}{\cdot}s^{-1}$. The threshold voltage, extracted by maximum transconductance extrapolation method, was approximately −7 V, and the subthreshold swing was estimated to be 358.89 mV dec^{-1}, which are consistent with typical values reported for AlGaN/GaN HEMT devices.

These findings demonstrate that the HEMT sensors not only exhibited a sensitive response to interfacial charge variations but also maintained robust stability under continuous testing conditions.

3.4. S-layer driven protein immobilization for improved antibody density

Building on a rational design strategy for functionalized biosensing interfaces, this investigation postulated that the S-layer architecture could enhance the antibody density on the sensor surface. To assess the packing density of biomolecules on the surface, surface plasmon resonance (SPR) was used to analyze the protein immobilization on gold surfaces.

Fig. 4a illustrates the immobilization procedure mediated by the self-assembly of the S-layer protein. The injection of the S-layer protein triggered a rapid increase in the response unit (RU) value upon reaching equilibrium. The surface coverage was essentially completed within 10 min approximately, as shown in Fig. 4b. Subsequent washing with PBST removed the unbound proteins from the surface, leading to a minor

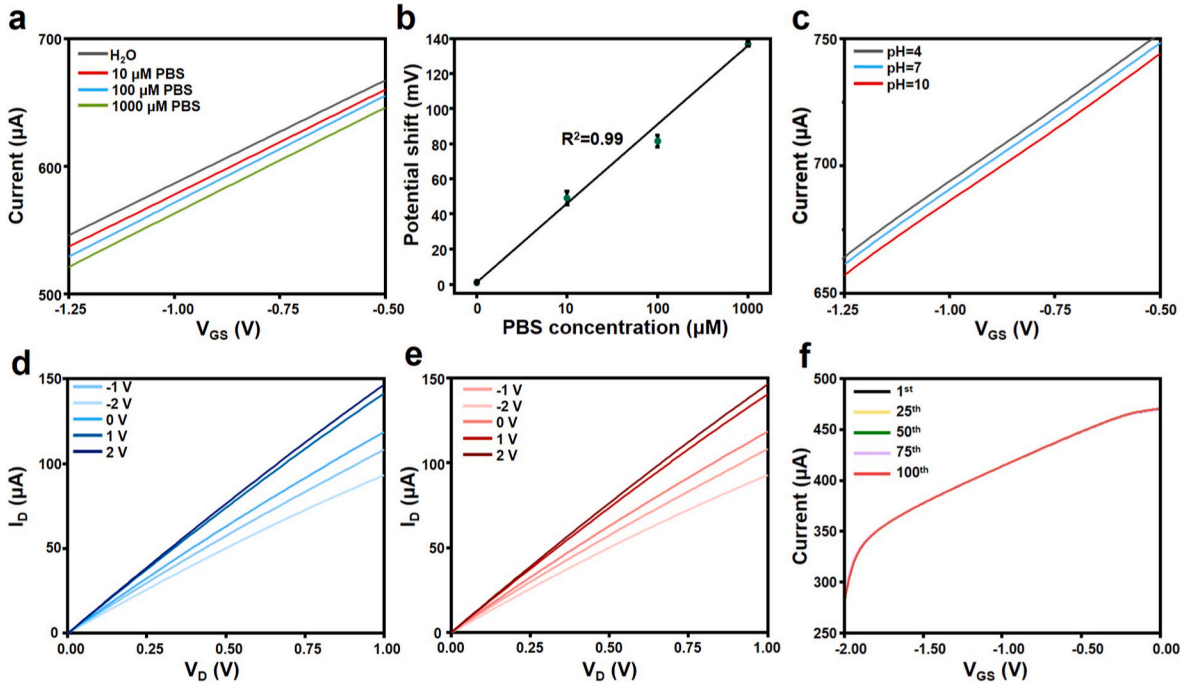

Fig. 3. Characterization of the electrical performance of HEMT sensor. (a) Transfer characteristic curves of the AlGaN/GaN HEMT sensor in PBS solutions with increasing concentrations from 10 μM to 1 mM. (b) Regression curves showing the potential shift in response to different PBS concentrations. (c) Transfer characteristic curves of the HEMT sensor in solutions with different pH values. (d) I–V curves from the first measurement cycle. (e) I–V curve from the 100th measurement cycle. (f) Continuous 100-cycle transfer curve measurements.

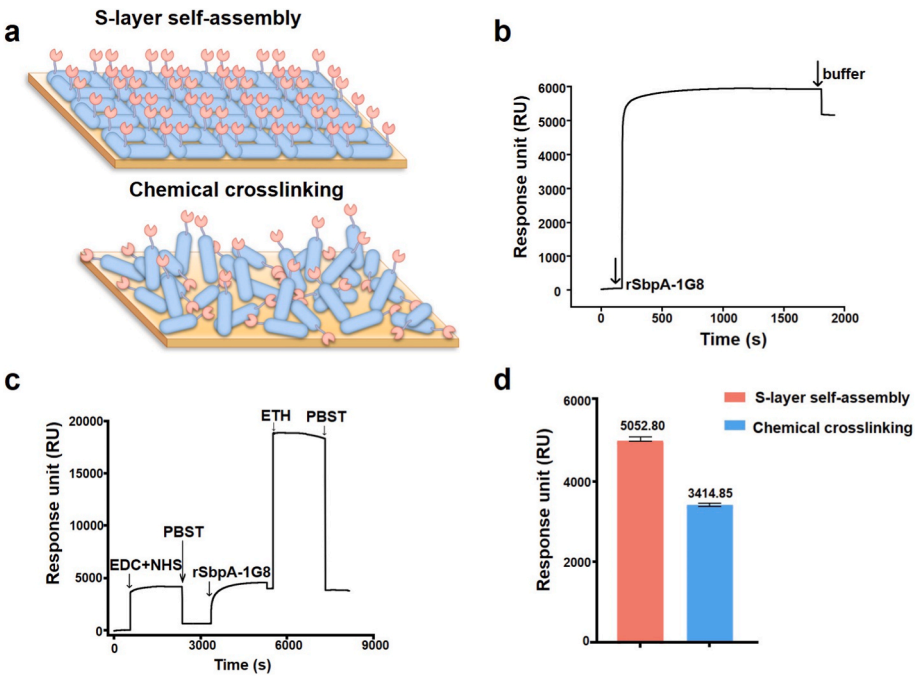

Fig. 4. Characterization of antibody density of functionalized sensor surfaces. (a) Schematic of the S-layer self-assembly and chemical crosslinking on the sensor surface. SPR analysis of protein immobilization process through the self-assembly of recombinant S-layer protein (b) and chemical crosslinking (c) on a gold chip. (d) SPR assessment of protein immobilization amount using different functionalization strategies based on three separate tests.

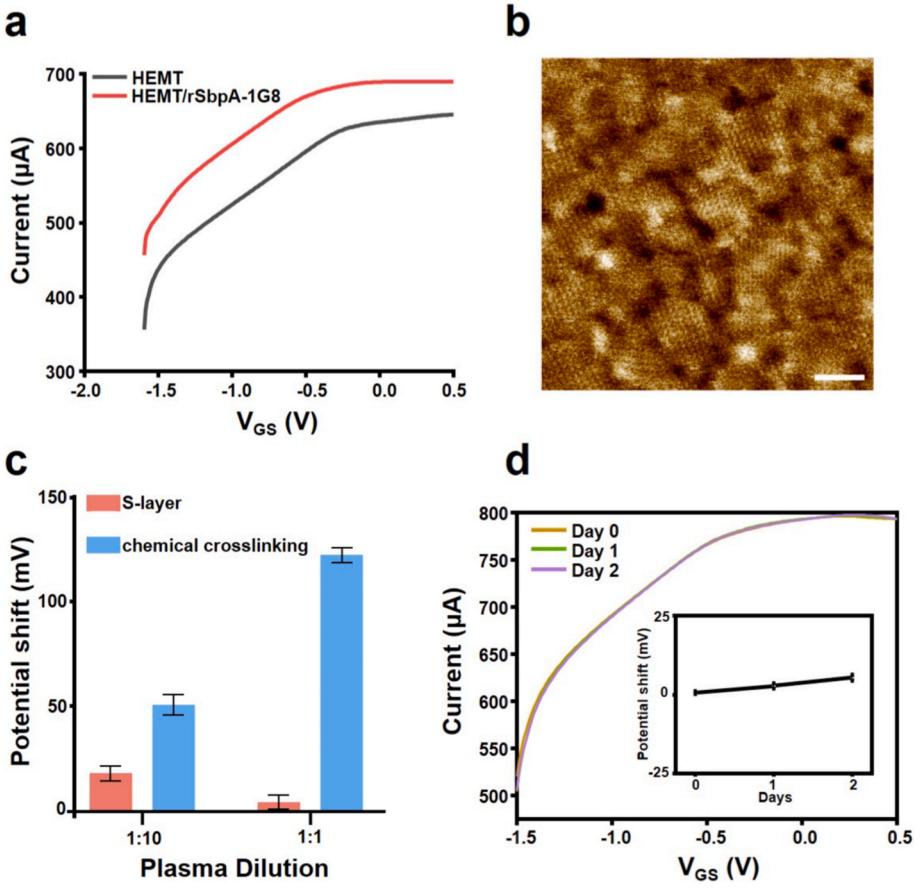

Fig. 5. Antifouling property and Stability of S-layer-based HEMT sensor. (a) Transfer characteristic curves of HEMT sensor before and after S-layer functionalization. (b) AFM images of gold interface modified by self-assembled S-layer protein, scale bar: 100 nm. (c) Potential shift produced by varying dilutions of plasma on the HEMT sensor surface, functionalized via the self-assembly of rSbpA-1G8 (red column) or chemical crosslinking (blue column). (d) Transfer characteristic curves of S-layer functionalized HEMT sensor recorded over a two-day period and the inset shows the corresponding potential shift observed over the same interval.

reduction in the RU value. In contrast, the conventional chemical crosslinking-based immobilization method involves multiple steps, including EDC/NHS activation, protein coupling, ethanolamine blocking, and several washing cycles, requiring more than 2 h to complete (Fig. 4c).

We quantitatively compared the protein immobilization efficiency of the S-layer-based method with that of the chemical crosslinking method. The S-layer approach yielded an average response of 5052.8 RU, which is nearly 50 % higher than the 3414.8 RU obtained with chemical crosslinking (Fig. 4d). Given the constrained surface area of the HEMT sensors, this enhanced protein-loading capacity directly amplifies nanobody-analyte interaction opportunities, thereby improving the sensitivity of HE4 detection and further improving the linear dynamic range.

3.5. Antifouling property and stability of S-layer-based HEMT sensor

Non-specific binding is a major obstacle to the clinical application of HEMT sensors. To address this issue, we functionalized the sensor surface with engineered S-layer proteins, and evaluated its resistance to non-specific adsorption. Recombinant rSbpA-1G8 was allowed to self-assemble on the device, and transfer characteristics were subsequently measured. The S-layer-coated sensor exhibited a pronounced shift of 569.8 mV at a drain current of 600 μA (Fig. 5a), confirming the successful immobilization of the recombinant protein. The AFM images (Fig. 5b) of S-layer proteins immobilized on gold substrates by chemical self-assembly, demonstrating successful formation of a monomolecular film with high density and structural regularity.

We then assessed the antifouling performance by directly exposing the S-layer-modified surface to bovine serum albumin (BSA), plasma. As shown in Fig. S4, the S-layer surface generated a negligible signal in the presence of BSA, while maintained substantially low non-specific adsorption in plasma (Fig. 5c). No obvious non-specific binding was observed for potential interfering proteins on the HEMT sensor surface (Fig. S5). In contrast, the sensor surface functionalized via chemical cross-linking, even after blocking with 1 mg/mL BSA, displayed extremely high non-specific binding. These results demonstrate that S-layer mediation effectively suppresses interfacial fouling, which is a critical factor for enhancing diagnostic accuracy.

To evaluate operational robustness, we recorded transfer characteristic curves over successive storage intervals in a liquid environment at 4 °C (Fig. 5d). The S-layer-functionalized HEMT sensor exhibited a

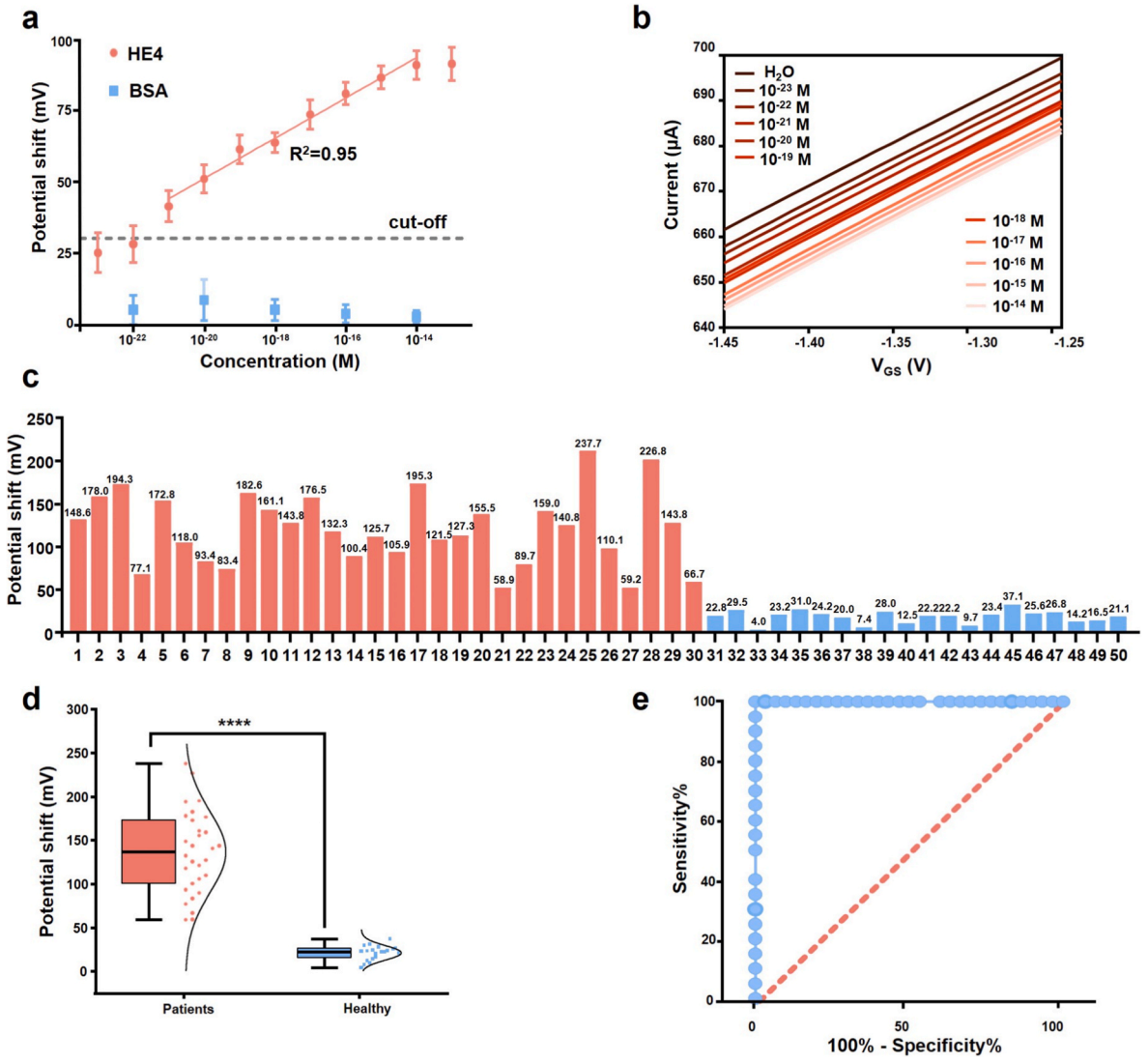

Fig. 6. Detection of purified HE4 and clinical samples using S-layer functionalized HEMT sensor. (a) Dependence of potential shift on protein concentration for both BSA and HE4. (b) Transfer characteristic curves measured at various HE4 protein concentrations. (c) Potential shift produced by plasma from 30 patients with ovarian cancer(red) and healthy individuals (blue). (d) Statistically significant difference in potential shift produced by patients with ovarian cancer and healthy individuals ($p < 0.0001$). (e) ROC curve analysis evaluating diagnostic performance.

potential shift of less than 5 mV over two days, and its output characterization curves remained stable (Fig. S6). Collectively, these findings underscore the excellent antifouling performance and stability of the S-layer based HEMT sensor, highlighting its potential for reliable real-world clinical applications.

3.6. Detection of purified HE4 and clinical sample using S-layer functionalized HEMT sensor

The S-layer functionalized HEMT sensor was initially evaluated for protein detection. As shown in Fig. 6a, the potential shift increased with increasing HE4 concentration, and the maximum potential shift was limited to 8.66 mV by BSA. The cutoff value was defined as the maximum potential shift induced by BSA plus three times the standard deviation corresponding to 30.3 mV. The results revealed that the S-layer-functionalized HEMT sensor could detect HE4 protein at concentrations as low as 10^{-21} M with a linear detection range for HE4 protein extending from 10^{-21} M to 10^{-14} M ($R^2 = 0.95$). The transfer curves produced at different concentrations of HE4 exhibited a rightward shift (Fig. 6b). In contrast, the exposure to varying concentrations of BSA elicited no significant response (Fig. S7). For comparison, HE4 detection was also performed on HEMT sensors functionalized by chemical crosslinking, where the minimum detectable concentration of HE4 was 10^{-18} M, with a linear detection range from 10^{-18} M to 10^{-13} M (Fig. S8). Our proposed method surpasses the sensitivity of conventional ELISA and even state-of-the-art detection methods (Chen et al., 2025). For example, a dual-signal electrochemiluminescence (ECL) immunosensor achieved a detection limit of 1.58 pg/mL for HE4, corresponding to 10^{-14} M (Tang et al., 2023), and a surface-enhanced Raman scattering (SERS) immunoassay based on gold nanoplates and nanoparticles enabled HE4 detection down to 10^{-17} M (Moothanchery et al., 2022).

The effect of plasma matrix was assessed prior to clinical measurements. Similar responses obtained from plasma diluted 1:1 and 1:10, suggesting the presence of matrix effects (Fig. S9). To normalize such effects, all clinical samples were measured using a fixed 1:10 dilution, enabling reliable comparative analysis between healthy individuals and patients. Then plasma samples from 30 patients with ovarian cancer and 20 healthy individuals were randomly selected for the analysis. As shown in Fig. 6c, the potential shift values recorded from plasma samples of patients with ovarian cancer were significantly higher than those from healthy individuals. Specifically, the average potential shift for healthy samples was 21.07 mV, whereas the plasma samples from patients with ovarian cancer exhibited an average potential shift of 136.2 mV, with values reaching up to 237.7 mV in some cases. Statistical analysis confirmed a significant difference in HE4 expression levels between patients with ovarian cancer and healthy individuals ($p < 0.001$; Fig. 6d). Moreover, a receiver operating characteristic (ROC) curve analysis yielded an area under the curve (AUC) of 1.0 (Fig. 6e), underscoring the excellent diagnostic accuracy of the S-layer-based HEMT sensor.

4. Conclusion

In summary, we developed an ultrasensitive biosensing platform by integrating recombinant bacterial S-layer proteins with an AlGaN/GaN HEMT sensor for the detection of the ovarian cancer biomarker HE4. The ordered S-layer architecture significantly enhanced antibody density while minimized nonspecific adsorption, enabling detection of HE4 at concentrations as low as 10^{-21} M, with a linear dynamic range spanning eight orders of magnitude (10^{-21}-10^{-14} M) and achieving 100 % diagnostic accuracy (AUC = 1.0). These results underscore the potential of S-layer-based HEMT biosensors for ultra-low-abundance biomarker detection, with broad implications for precision diagnostics in cancer and other diseases. Future efforts focusing on expanding the antibody repertoire for multiplexed detection and advancing device miniaturization into portable, multichannel systems will be essential to translate this platform into high-throughput, point-of-care cancer screening.

CRediT authorship contribution statement

Jingya Tang: Writing – original draft, Methodology, Investigation, Conceptualization. **Chenyang Yang:** Writing – original draft, Methodology, Investigation, Conceptualization. **Jianwen Sun:** Resources, Methodology. **Zhe Li:** Resources. **Yue Men:** Methodology, Investigation. **Zewen Liu:** Resources, Methodology, Conceptualization. **Guoqi Zhang:** Resources, Conceptualization. **Xian-En Zhang:** Writing – review & editing, Supervision, Funding acquisition, Conceptualization. **Dian-Bing Wang:** Writing – review & editing, Writing – original draft, Supervision, Funding acquisition, Conceptualization.

Funding

This work was supported by the National Key Research and Development Program of China (Grant No. 2022YFA1205804 and 2022YFC2303501, and the National Natural Science Foundation of China (Grant No. 32271489).

Declaration of competing interest

The authors declare that they have no known competing financial interests or personal relationships that could have appeared to influence the work reported in this paper.

Acknowledgments

Special thanks to Boling Zhu of the Institute of Biophysics, Chinese Academy of Sciences for assisting with the TEM experiments.

Appendix A. Supplementary data

Supplementary data to this article can be found online at https://doi.org/10.1016/j.bios.2026.118382.

Data availability

Data will be made available on request.

References

Chen, X., et al., 2021. Nat. Commun. 12, 5506. https://doi.org/10.1101/2020.10.29.361287.
Chen, M.-N., et al., 2025. J. Electrochem. Soc. 172. https://doi.org/10.1149/1945-7111/ada580.
Chu, C.H., et al., 2017. Sci. Rep. 7, 1–15. https://doi.org/10.1038/s41598-017-05426-6.
Grill, W., et al., 2025. J. Biol. Chem. 301. https://doi.org/10.1016/j.jbc.2025.110205.
Guo, K., et al., 2023. Adv. Sci., 2306716 https://doi.org/10.1002/advs.202306716, 1–13.
Hemaja, V., et al., 2022. Silicon 14, 1873–1886. https://doi.org/10.1007/s12633-020-00937-w.
Hwang, M.T., et al., 2020. Nat. Commun. 11, 1543. https://doi.org/10.1038/s41467-020-15330-9.
J, F.O., et al., 2008. N. Engl. J. Med. 358, 2704–2715. https://doi.org/10.1056/nejmra072739.
Kaisti, M., 2017. Biosens. Bioelectron. 98, 437–448. https://doi.org/10.1016/j.bios.2017.07.010.
Kakasi, B., et al., 2023. BMC Res. Notes 16, 110. https://doi.org/10.1186/s13104-023-06382-3.
Kang, H., et al., 2021. Nano Lett. 21, 7897–7904. https://doi.org/10.1021/acs.nanolett.1c00837.
Karami, E., et al., 2020. J. Drug Deliv. Sci. Technol. 55, 101471. https://doi.org/10.1016/j.jddst.2019.101471.
Lavinia, G., et al., 2024. eLife 13, e84617. https://doi.org/10.7554/eLife.84617.
Liu, J., et al., 2021. Int. J. Biol. Macromol. 166, 884–892. https://doi.org/10.1016/j.ijbiomac.2020.10.245.
Moll, D., et al., 2002. Proc. Natl. Acad. Sci. U. S. A 99, 14646–14651. https://doi.org/10.1073/pnas.232299399.
Moothanchery, M., et al., 2022. Sci. Rep. 12. https://doi.org/10.1038/s41598-022-13859-x.

Pallares, R.M., et al., 2022. J. Am. Chem. Soc. 144, 854–861. https://doi.org/10.1021/jacs.1c10802.
Qing, R., et al., 2023. Sci. Adv. 9, 1–13. https://doi.org/10.1126/sciadv.adf1402.
Reth, M., 2013. Nat. Immunol. 14, 765–767. https://doi.org/10.1038/ni.2621.
Sarangadharan, I., et al., 2018. Biosens. Bioelectron. 100, 282–289. https://doi.org/10.1016/j.bios.2017.09.018.
Schuster, B., 2018. Biosensors 8, 40. https://doi.org/10.3390/bios8020040.
Seo, G., et al., 2020. ACS Nano 14, 5135–5142. https://doi.org/10.1021/acsnano.0c02823.
Sleytr, U.B., et al., 2007. FEBS J. 274, 323–334. https://doi.org/10.1111/1574-6976.12063.
Tang, J., et al., 2022. Anal. Chem. 94, 9355–9362. https://doi.org/10.1021/acs.analchem.2c01190.
Tang, Y., et al., 2023. Anal. Chem. 95, 4795–4802. https://doi.org/10.1021/acs.analchem.3c00273.
Vacic, A., et al., 2011. J. Am. Chem. Soc. 133, 13886–13889. https://doi.org/10.1021/ja205684a.
Wang, X.Y., et al., 2015. Small 11, 5826–5832. https://doi.org/10.1002/smll.201501413.
Woo, K., et al., 2020. Biosens. Bioelectron. 159, 112186. https://doi.org/10.1016/j.bios.2020.112186.
Wu, Y., et al., 2019. J. Am. Chem. Soc. 141, 1162–1170. https://doi.org/10.1021/jacs.8b09397.
Wu, Y., et al., 2020. Chem. Sci. 11, 12570–12579. https://doi.org/10.1039/d0sc04552g.
Yang, Y., et al., 2022. Adv. Mater. 34, 1–13. https://doi.org/10.1002/adma.202203224.
Yang, C., et al., 2024. Biosens. Bioelectron. 257, 116171. https://doi.org/10.1016/j.bios.2024.116171.
Yu, J., et al., 2022. Int. J. Biol. Macromol. 199, 298–306. https://doi.org/10.1016/j.ijbiomac.2022.01.015.
Zhang, Q., et al., 2016. J. Clin. Lab. Anal. 30, 709–718. https://doi.org/10.1002/jcla.21926.
Zhang, Y., et al., 2023. Adv. Mater., 2306252 https://doi.org/10.1002/adma.202306252, 1–19.
Zhang, Q., et al., 2024. Adv. Sci. 11, 2401796. https://doi.org/10.1002/advs.202401796.
Zhou, Y., et al., 2024. Signal Transduct. Targeted Ther. 9, 132. https://doi.org/10.1038/s41392-024-01823-2.